Streaming by leaky surface acoustic waves

J Vanneste* and O Bühler†

†School of Mathematics and Maxwell Institute for Mathematical Sciences
University of Edinburgh, Edinburgh EH9 3JZ, UK

*Courant Institute of Mathematical Sciences
New York University, New York, NY 10012, USA

Acoustic streaming, the generation of mean flow by dissipating acoustic waves, provides a promising method for flow pumping in microfluidic devices. In recent years, several groups have been experimenting with acoustic streaming induced by leaky surface waves: (Rayleigh) surface waves excited in a piezoelectric solid interact with a small volume of fluid where they generate acoustic waves and, as result of the viscous dissipation of these waves, a mean flow. We discuss the computation of the corresponding Lagrangian mean flow, which controls the trajectories of fluid particles and hence the mixing properties of the flows generated by this method.

The problem is formulated using the averaged vorticity equation. This extracts the balance between wave dissipation and mean-flow dissipation that is at the core of the streaming process by eliminating large, cancelling terms in the averaged momentum equation. Particular attention is paid to the thin boundary layer that forms at the solid/liquid interface, where both the acoustic waves and their streaming effect are best computed using matched asymptotics. This leads to an explicit expression for a slip velocity which gives the limiting value of the Lagrangian mean velocity away from the boundary; this expression generalises earlier results by including the effect of the oscillations of the boundary.

The Lagrangian mean flow is naturally separated into three contributions: an interior-driven Eulerian mean flow, a boundary-driven Eulerian mean flow, and the Stokes drift. A scale analysis indicates that the latter two contributions can be neglected in devices much larger than the acoustic wavelength but need to be taken into account in smaller devices. A simple two-dimensional model of mean-flow generation by surface acoustic waves is discussed as an illustration.

1 Introduction

The numerous applications of microfluidic technology, in biology and chemistry in particular, have stimulated a great deal of research about the physics of fluids at small scales (see, e.g., Nguyen & Wereley (2002), Squires & Quake (2005) or Tabeling (2006) for an introduction). Many microfluidic devices require to mix reacting solutions efficiently. As is well recognised,

this poses a challenge because the small values of the diffusivity of most chemicals make molecular diffusion impractically slow, while the low Reynolds numbers in typical devices preclude turbulent mixing. Much effort has therefore been devoted to the design of efficient micromixers, which typically rely on the formation of small-scale structures in the concentration fields to enhance the effect of molecular diffusion. (The references above discuss several examples of micromixers.)

Although small-scale structures can be generated in steady flows, they develop much more rapidly in time-dependent flows through the process of chaotic advection (see, e.g., Wiggins & Ottino 2004, and other articles in the same journal issue). It is therefore highly desirable to develop methods for the stirring of microfluids that are flexible enough to generate time-dependent flows while interfering as little as possible with whatever chemical or biological processes might take place. One particularly attractive type of such methods is based on acoustic waves: (ultra)sound waves propagating in a fluid induce a time-averaged flow (or mean flow) through the nonlinear process known as acoustic streaming (e.g. Lighthill 1978*a*,*b*). Time-dependent mean flows can readily be obtained by varying the frequency of the waves and/or the location of the wave sources.

The potential of these methods has been demonstrated in a number of experiments (Moroney et al. 1991, Suri et al. 2002, Wixforth 2003, Guttenberg et al. 2004, Sritharan et al. 2006, Frommel et al. 2008*a*, Tan et al. 2009, Du et al. 2009, Yeo & Friend 2009). Most of these experiments share the same method of excitation of acoustic waves in the fluid, based on leaky surface acoustic waves (LSAWs). Surface acoustic waves (Rayleigh waves) are generated in a solid substrate by piezoelectric excitation. These waves propagate along the surface of the solid and, when this is contact with a fluid above, radiate (leak) energy into the fluid in the form of acoustic waves. In turn, these waves generate a mean flow by acoustic streaming.

In this paper, we consider this physical mechanism and discuss its mathematical modelling. Several recent papers complement the experimental work with numerical simulations of the LSAWs and of the mean flow they generate (Frommel et al. 2008*b*, Köster 2007, Tan et al. 2009, Antil et al. 2010). To compute the mean flow, these papers implement the formulation of Nyborg (1953, 1965) based on the time-averaged momentum equation. This formulation has the disadvantage of ignoring the implications of vorticity conservation: as other mechanisms of wave–mean flow interaction (e.g. Bühler 2009), acoustic streaming in a homogeneous fluid is strongly constrained by the fact that vorticity cannot be generated by purely inviscid processes. As a result, the mean flow forcing by acoustic waves depends entirely on dissipative processes. Because of the high frequency of the waves involved (typically in the range 0.1–1 GHz), these processes are very weak: indeed, the averaged momentum equation is completely dominated by the inviscid stress and pressure terms, which however balance and hence do not contribute to mean-flow generation. To make this explicit, we use here the averaged vorticity equation in place of the momentum equation, following the original formulation of Eckart (1948) and Westervelt (1953). This formulation isolates the balance between the dissipation of the waves and of the mean flow which controls the streaming, and leads to the well-known observation that the streaming flow is independent of the value of the viscosity (or, more precisely, depends

only on the ratio of the shear viscosity to the bulk viscosity). The vorticity formulation is particularly advantageous for the problem at hand because the mean flow is non-divergent up to negligible terms.

There are two forms of acoustic streaming whose relative contribution to mean-flow generation depends on the size of the devices. *Interior streaming* is associated with the vorticity that appears when the irrotational acoustic waves dissipate in the fluid's interior. *Boundary streaming*, on the other hand, is associated with a vortical part of the acoustic waves which is confined to thin boundary layers. To date, the boundary contribution to streaming in LSAW devices has received little attention (see Tan et al. 2009, however). In this paper, we consider both forms of streaming. We provide explicit expressions for the wave and mean-flow structure inside the boundary layers and hence obtain the slip velocity that can be used as boundary condition for the averaged vorticity equation. Because the boundaries of LSAW devices are oscillating, this requires extending the standard analysis of boundary streaming (e.g. Lighthill 1978*a*) in a manner analogous to Longuet-Higgins's (1953) treatment of incompressible flows.

The main point of interest in the study of LSAW micromixers is the mean motion of particles in the fluid. This is governed by the Lagrangian mean flow which sums the Eulerian mean flow discussed above with the Stokes drift (e.g. Bühler 2009). The Stokes drift, which results from the nonlinearity of the advection equation, contributes directly to the mean advection; it also impacts on the Eulerian mean flow through boundary conditions, since it is the total Lagrangian mean flow, not the Eulerian mean flow, that satisfies no-slip boundary conditions (e.g. Bradley 1996).

The paper is organised as follows. In § 2, we present the compressible Navier–Stokes equations used to model the fluid, introduce their small-amplitude expansion, and define the mean flows to be evaluated. Section 3 discusses a solution procedure yielding the form of the acoustic waves in the fluid interior and near the boundary while taking advantage of the small viscosity/high frequency of typical LSAW devices. The Eulerian and Lagrangian mean flows are considered in § 4. The averaged vorticity equation governing the interior mean flow is derived, and the slip velocity is computed from the boundary-layer solution. The modelling of the solid supporting the LSAWs is described in § 5: for simplicity, we restrict ourselves to a simple two-dimensional configuration and treat the solid as a linear elastic isotropic material. We pay particular attention to the boundary conditions to be applied at the (moving) interface between the solid and the liquid. Section 6 presents results for this configuration with a choice of physical parameters that correspond to the experiments mentioned above. We emphasise the importance of the size of the LSAW device for the relative contributions of the interior and boundary streamings to the Lagrangian mean flow. The paper concludes with a discussion in § 7. Two appendices give details of the numerical method employed, and the boundary-layer analysis; a third appendix briefly considers the mean flows in a completely inviscid situation.

2 Formulation

The fluid is modelled by the compressible Navier–Stokes equations

$$\rho\left(\partial_t \boldsymbol{u} + \boldsymbol{u}\cdot\nabla\boldsymbol{u}\right) = -\nabla p + \mu\nabla^2\boldsymbol{u} + \mu'\nabla\nabla\cdot\boldsymbol{u}, \tag{2.1}$$

$$\partial_t\rho + \nabla\cdot\left(\rho\boldsymbol{u}\right) = 0, \tag{2.2}$$

for the fluid's velocity $\boldsymbol{u}$, density ρ and pressure p (e.g. Landau & Lifschitz 1987). Here, μ is the shear viscosity and μ' is related to the shear viscosity and bulk viscosity μ^{b} by

$$\mu' = \mu^{\mathrm{b}} + \mu/3.$$

Both the shear and bulk viscosities contribute substantially to the dissipation of acoustic waves and need to be taken into account (e.g Lighthill 1978*b*). Here we ignore thermal effects and in particular the thermal dissipation of acoustic waves; this is appropriate for liquids, but not for gases. We also assume that μ and μ^{b} are constant. Equations (2.1)–(2.2) are complemented by an equation of state

$$p = p(\rho). \tag{2.3}$$

Since the phenomenon of interest is usually characterised by small wave amplitudes, we can simplify (2.1)–(2.3) using a perturbation expansion based on a formal parameter $\alpha \ll 1$. Thus, we introduce expansions of the form

$$\boldsymbol{u} = \alpha\boldsymbol{u}_1 + \alpha^2\boldsymbol{u}_2 + O(\alpha^3), \tag{2.4}$$

$$\rho = \rho_0 + \alpha\rho_1 + \alpha^2\rho_2 + O(\alpha^3), \tag{2.5}$$

$$p = \alpha p_1 + \alpha^2 p_2 + O(\alpha^3), \tag{2.6}$$

where ρ_0 is a constant, into the equations.

We assume a time-harmonic forcing with (angular) frequency ω. The $O(\alpha)$ solution, which we term the wave solution, can then be written in the form

$$\boldsymbol{u}_1 = \hat{\boldsymbol{u}}\mathrm{e}^{-\mathrm{i}\omega t} + \text{c.c.}, \tag{2.7}$$

where c.c. denotes the complex conjugate of the previous term. Similar expressions hold for ρ and p. The hatted fields are time-independent, complex fields which are computed in § 3 below. Once they are determined, the $O(\alpha^2)$ fields generated nonlinearly can be obtained. Our focus is on the time-averaged response, and specifically on the Eulerian mean velocity

$$\bar{\boldsymbol{u}}^{\mathrm{E}} = \bar{\boldsymbol{u}}_2, \tag{2.8}$$

where the overbar denotes time average, and on the Stokes drift

$$\bar{\boldsymbol{u}}^{\mathrm{S}} = \overline{\boldsymbol{\xi}_1\cdot\nabla\boldsymbol{u}_1}. \tag{2.9}$$

Both the Eulerian mean flow and Stokes drift contribute at the same order to the Lagrangian mean velocity

$$\bar{\boldsymbol{u}}^{\mathrm{L}} = \bar{\boldsymbol{u}}^{\mathrm{E}} + \bar{\boldsymbol{u}}^{\mathrm{S}}, \tag{2.10}$$

which gives the average motion of particles in the fluids to $O(\alpha^2)$ (e.g. Bühler 2009). Note that

$$\rho_0 \bar{\boldsymbol{u}}^{\mathrm{L}} = \rho_0 \bar{\boldsymbol{u}}_2 + \overline{\rho_1 \boldsymbol{u}_1} + \rho_0 \nabla \cdot \left(\overline{\boldsymbol{\xi}_1 \otimes \boldsymbol{u}_1} \right), \tag{2.11}$$

where the divergence term vanishes only in special circumstances. Thus $\rho_0 \bar{\boldsymbol{u}}^{\mathrm{L}}$ is not necessarily the $O(\alpha^2)$ approximation to the mean mass flux $\overline{\rho \boldsymbol{u}}$.

3 Acoustic waves

We now introduce the expansions (2.4)–(2.6) into (2.1)–(2.2) and collect the $O(\alpha)$ terms. Using the Helmholtz decomposition into irrotational and divergence-free flow

$$\boldsymbol{u}_1 = \nabla \phi_1 + \nabla \times \boldsymbol{\psi}_1, \quad \text{with} \;\; \nabla \cdot \boldsymbol{\psi}_1 = 0, \tag{3.1}$$

we obtain, after some manipulations, the damped wave equation

$$\partial_{tt}^2 \phi_1 = c^2 \nabla^2 \phi_1 + (\nu + \nu') \partial_t \nabla^2 \phi_1 \tag{3.2}$$

for the scalar potential ϕ_1, and the equation

$$\partial_t \left(\nabla \times \boldsymbol{\psi}_1 \right) = \nu \nabla^2 \left(\nabla \times \boldsymbol{\psi}_1 \right) \tag{3.3}$$

for the vector potential (e.g. Nyborg 1965). Here we have introduced the kinematic viscosities $\nu = \mu/\rho_0$ and $\nu' = \mu'/\rho_0$, and the sound speed

$$c^2 = \left. \frac{\mathrm{d}p}{\mathrm{d}\rho} \right|_0 . \tag{3.4}$$

In the absence of interior forcing, the vorticity $\nabla^2 \boldsymbol{\psi}_1$ is exponentially confined near the boundaries of the fluid, so that the wave solution in the interior of the fluid is irrotational. If the viscosity is small, the computation of the wave solution can therefore be much simplified using matched asymptotics. The condition for this to apply is that the boundary-layer thickness, given by

$$\delta = \sqrt{\frac{2\nu}{\omega}}, \tag{3.5}$$

be much smaller than the inverse wavenumber of the acoustic waves, κ^{-1} say. In typical applications of LSAW-induced flows in water, ω is in the range 0.1–1 GHz and we estimate that δ is of the order of 40 nm; correspondingly, $\delta\kappa = \sqrt{2\nu\omega}/c$ is of the order of 10^{-2}, so that an asymptotic treatment of the wave problem is well justified. The smallness of $\delta\kappa$ also implies that the waves are only weakly dissipated in the fluid interior: solving (3.2) for plane waves gives their spatial damping rate as

$$\gamma = \frac{(\nu + \nu')\kappa^2}{2c} = \frac{\nu + \nu'}{4\nu} \delta^2 \kappa^3 \tag{3.6}$$

(Nyborg 1965). Thus $\delta\kappa \ll 1$ clearly implies that $\gamma/\kappa \ll 1$, corresponding to weak interior dissipation. The viscous dissipation of the waves is however significant for the wave solution in

devices whose size is of the order γ^{-1} or larger; it is also key to the mean-flow generation. Note that the boundary layer is much thicker than the typical fluid-particle displacements associated with the LSAWs, which are of the order of a nanometer or less. Therefore the condition $\delta\kappa \ll \alpha$, required to expand the equations in powers of α before expanding in δ, is met.

Taking advantage of the smallness of $\delta\kappa$ gives a straightforward procedure for the computation of the wave solution. First the time-harmonic version of (3.2), namely

$$\nabla^2\hat{\phi} = -\frac{\omega^2}{c^2 - \mathrm{i}(\nu+\nu')\omega}\hat{\phi} \tag{3.7}$$

is solved, to obtain the potential part of the wave field. It is not appropriate here to neglect the viscous term since the solution needs to be valid over distances that may be large compared to γ^{-1}. The boundary conditions, however, are those appropriate for an inviscid fluid: no normal flow across the boundary and, in the case of a dynamic boundary, continuity of normal stress and zero tangential stress (see § 5 below). The result, then, is an approximation to the exact potential $\hat{\phi}$, with $O(\delta\kappa)$ errors stemming from the approximate boundary conditions.

Once this approximation to $\hat{\phi}$ is obtained, the leading-order, $O(\delta\kappa)$ vector potential $\hat{\boldsymbol{\psi}}_1$ is found by solving (3.3) using a boundary-layer approach of the type pioneered by Rayleigh (1896, art. 352). This part of the solution ensures that the tangential velocity in the fluid also matches that of the boundary. Consistent with the linearisation leading to (3.2)–(3.3), the boundary conditions are imposed at the undisturbed location of the boundary in the case of a dynamic boundary.

Let us consider for example a solid boundary at $z = 0$ that is possibly oscillating with velocity $\boldsymbol{u}^{\mathrm{s}}(x, y, 0, t) = \hat{\boldsymbol{u}}^{\mathrm{s}}(x, y, 0)\exp(-\mathrm{i}\omega t) + \mathrm{c.c.}$. The fluid velocity is written as

$$\boldsymbol{u}_1(x, y, z) = \nabla\phi_1(x, y, z) + \delta\nabla \times \boldsymbol{\Psi}_1(x, y, z/\delta), \tag{3.8}$$

with a contribution of the vector potential that decreases exponentially as

$$Z = z/\delta \tag{3.9}$$

tends to ∞. The scaling (3.8) ensures that the leading-order contribution of the divergence-free flow is the $O(1)$ tangential velocity needed to enforce the no-slip boundary condition.

To leading order, the three components of the velocity in the boundary layer thus have the form

$$u_1 = \partial_x\phi_1 - \partial_Z\Psi^{(2)} + O(\delta), \quad v_1 = \partial_y\phi_1 + \partial_Z\Psi^{(1)} + O(\delta) \ \text{ and } \ w_1 = \partial_z\phi_1 + O(\delta), \tag{3.10}$$

where we have written the components of the vector potential as

$$\boldsymbol{\Psi}_1 = (\Psi^{(1)}, \Psi^{(2)}, \Psi^{(3)})$$

and used $O(\delta)$ as a shorthand for $O(\delta\kappa)$. Introducing (3.8) into (3.3), we obtain the leading-order equations

$$\partial^3_{ZZZ}\hat{\Psi}^{(j)} + 2\mathrm{i}\partial_Z\hat{\Psi}^{(j)} = 0, \quad j = 1,\, 2.$$

The solutions which decay as $Z \to \infty$ and ensure the continuity of the tangential components of the velocity are

$$\partial_Z \hat{\Psi}^{(2)}(x,y,Z) = \hat{U}(x,y)\mathrm{e}^{-(1-\mathrm{i})Z} \quad \text{and} \quad \partial_Z \hat{\Psi}^{(1)}(x,y,Z) = -\hat{V}(x,y)\mathrm{e}^{-(1-\mathrm{i})Z}, \tag{3.11}$$

where we have introduced the two components

$$\hat{U}(x,y) = \partial_x \hat{\phi}(x,y,0) - \hat{u}^{\mathrm{s}}(x,y,0) \quad \text{and} \quad \hat{V}(x,y) = \partial_y \hat{\phi}(x,y,0) - \hat{v}^{\mathrm{s}}(x,y,0) \tag{3.12}$$

of the difference between the tangential velocity of the potential flow in the fluid and the tangential velocity of the solid.

Note that by (3.5) the viscous stress associated with the divergence-free flow, dominated by terms of the form $\mu\partial_z u_1 \sim \mu\delta^{-1}\partial_{ZZ}^2\Psi^{(2)}$, is $O(\delta)$ and hence negligible to leading order. This confirms the validity of imposing zero tangential stress at the boundary in the case of a dynamic boundary.

4 Mean flow

We now turn to the determination of the Lagrangian mean flow $\bar{\boldsymbol{u}}^{\mathrm{L}}$ induced by the acoustic waves in the fluid. The Stokes drift contribution to $\bar{\boldsymbol{u}}^{\mathrm{L}}$ can be computed straightforwardly from the wave fields found in § 3. The Eulerian flow $\bar{\boldsymbol{u}}^{\mathrm{E}}$, on the other hand, is determined by solving the time averaged Navier–Stokes equations (2.1)–(2.2) to order $O(\alpha^2)$. We emphasise that the Eulerian mean flow depends in an essential manner on the presence of a viscous dissipation of the acoustic waves: for an inviscid fluid, the Reynolds stresses associated with the wave-part of the solution are exactly balanced by a pressure gradient and there is no mean-flow forcing in the interior of the fluid (e.g Lighthill 1978*b*).[1] When the viscous effects are small (in the sense that $\delta\kappa \ll 1$ as is assumed here), this balance holds approximately and dominates the averaged momentum equation. This equation is therefore not well suited for the computation of the mean-flow forcing, which is several orders of magnitude smaller than the Reynolds stress and pressure gradient. Instead, we follow Eckart (1948) and Westervelt (1953) and use the averaged vorticity equation. Because the acoustic waves are essentially irrotational in the fluid interior, this equation takes a very simple form, one that isolates the mean-flow forcing and makes explicit that the mean-flow response depends on the ratio μ^{b}/μ and not on μ and μ^{b} separately.

Since the acoustic waves have vorticity in the boundary layers, the mean-flow generation there is controlled by a different balance than in the interior. An expression for the mean flow in the boundary layer is derived below; its limit away from the boundary layer provides the boundary condition that is needed for the interior in the form of a slip velocity. It is then convenient to separate the Eulerian mean flow in two contributions: the interior-driven contribution, which solves the interior equation with no-slip boundary condition, and the boundary-driven contribution, which solves a homogeneous interior equation with imposed slip boundary condition. The two contributions are both $O(1)$ in δ, but the interior-driven flow dominates in devices that are much larger than the wavelength of the acoustic waves.

[1] That is not to say that there is no Eulerian flow in the inviscid case, however; see Appendix C.

4.1 Interior

We start by considering the mean-flow equations away from the boundaries. Averaging (2.2) and using the important property

$$\overline{\partial_t(\,\cdot\,)} = 0 \tag{4.1}$$

leads to $\nabla\cdot(\rho_0\bar{\boldsymbol{u}}_2 + \overline{\rho_1\boldsymbol{u}_1}) = 0$. Taking the divergence of (2.11) and noting that

$$\nabla\cdot\left(\nabla\cdot\left(\overline{\boldsymbol{\xi}_1\otimes\boldsymbol{u}_1}\right)\right) = \partial^2_{ij}\left(\overline{\xi_{1i}u_{1j}}\right) = \frac{1}{2}\partial^2_{ij}\left(\overline{\partial_t(\xi_{1i}\xi_{1j})}\right) = 0,$$

where we have used Einstein's notation, then gives

$$\nabla\cdot\bar{\boldsymbol{u}}^{\mathrm{L}} = 0. \tag{4.2}$$

On the other hand, it follows from the definition of the Stokes drift and the irrotational nature of $\boldsymbol{u}_1$ that

$$\begin{aligned}\nabla\cdot\bar{\boldsymbol{u}}^{\mathrm{S}} &= \partial_i\left(\overline{\xi_{1j}\partial_j u_{1i}}\right) = \partial_i\left(\overline{\xi_{1j}\partial_i u_{1j}}\right) = \overline{\xi_{1j}\partial^2_{ii}u_{1j}} + \overline{\partial_i\xi_{1j}\partial_i u_{1j}}\\ &= \overline{\boldsymbol{\xi}_1\cdot\nabla^2\boldsymbol{u}_1} + \overline{\partial_i\xi_{1j}\partial_t(\partial_i\xi_{1j})} = c^{-2}\overline{\boldsymbol{\xi}_1\cdot\partial^2_{tt}\boldsymbol{u}_1} + O(\delta^2),\end{aligned}$$

using (3.2) and (4.1). Integrating by parts using (4.1) leads to

$$\nabla\cdot\bar{\boldsymbol{u}}^{\mathrm{S}} = O(\delta^2), \tag{4.3}$$

and hence to

$$\nabla\cdot\bar{\boldsymbol{u}}^{\mathrm{E}} = O(\delta^2). \tag{4.4}$$

Since we are interested only in the mean flow to leading-order in δ, we can now focus on the Eulerian mean vorticity $\nabla\times\bar{\boldsymbol{u}}^{\mathrm{E}}$: its knowledge in the fluid interior, together with (4.4) and boundary conditions determine $\bar{\boldsymbol{u}}^{\mathrm{E}}$ entirely.

We derive an equation for the Eulerian mean vorticity by first taking the curl of (2.1) to obtain

$$\partial_t\boldsymbol{\zeta} + \boldsymbol{u}\cdot\nabla\boldsymbol{\zeta} - \boldsymbol{\zeta}\cdot\nabla\boldsymbol{u} + \boldsymbol{\zeta}\nabla\cdot\boldsymbol{u} = \frac{\mu}{\rho}\nabla^2\boldsymbol{\zeta} - \frac{\mu}{\rho^2}\nabla\rho\times\nabla^2\boldsymbol{u} - \frac{\mu'}{\rho^2}\nabla\rho\times\nabla(\nabla\cdot\boldsymbol{u}), \tag{4.5}$$

where $\boldsymbol{\zeta} = \nabla\times\boldsymbol{u}$ is the vorticity. We then introduce the expansions (2.4)–(2.6) and average. Since the $O(\alpha)$ flow is irrotational in the interior, i.e. $\boldsymbol{\zeta}_1 = \nabla\times\boldsymbol{u}_1 = \nabla^2\boldsymbol{\Psi}_1 = 0$ there, the result is

$$0 = \frac{\mu}{\rho_0}\nabla^2\nabla\times\bar{\boldsymbol{u}}^{\mathrm{E}} - \frac{\mu}{\rho_0^2}\overline{\nabla\rho_1\times\nabla^2\boldsymbol{u}_1} - \frac{\mu'}{\rho_0^2}\overline{\nabla\rho_1\times\nabla(\nabla\cdot\boldsymbol{u}_1)}.$$

This can be further simplified into

$$\nabla^2\nabla\times\bar{\boldsymbol{u}}^{\mathrm{E}} = \frac{\nu+\nu'}{\rho_0^2\nu}\nabla\times\overline{\partial_t\rho_1\nabla\rho_1}, \tag{4.6}$$

using again that $\nabla\times\boldsymbol{u}_1 = 0$. This is the form obtained by Eckart (1948)and Westervelt (1953). A convenient alternative is to (4.6) is obtained using that $\boldsymbol{u}_1$ satisfies a wave equation up to $O(\delta^2)$ terms and reads

$$\nabla^2\nabla\times\bar{\boldsymbol{u}}^{\mathrm{E}} = -\frac{\nu+\nu'}{\nu}\frac{\omega^2}{\rho_0 c^2}\nabla\times\overline{\rho_1\boldsymbol{u}_1} + O(\delta^2). \tag{4.7}$$

In this form, the Eulerian mean flow forcing is directly related to the acoustic energy flux $c^2\overline{\rho_1 \boldsymbol{u}_1}$.

In what follows, we use (4.4) and (4.7) to compute the Eulerian mean flow $\bar{\boldsymbol{u}}^{\mathrm{E}}$ generated by LSAWs. As mentioned, this formulation has the advantage over the direct use of the averaged momentum equation of making explicit that the Eulerian mean flow is forced by the viscous dissipation of the acoustic waves. Since this forcing is balanced by viscosity, the Eulerian mean flow is independent of viscosity or, rather, dependent on the ratio ν'/ν (or equivalently μ^{b}/μ) only. In practice, we expect that the solution of (4.4) and (4.7) is a better conditioned problem than the solution of the averaged momentum equation: in the latter, the averaged wave stresses are balanced at $O(1)$ by pressure gradients so that only the much smaller $O(\delta^2)$ terms involving viscous effects matter to determine the Eulerian mean flow. The boundary conditions for (4.7) are found next by considering the boundary layers.

4.2 Boundary layers

Near the boundaries, the full $O(\alpha)$ velocity field of the form (3.10) needs to be taken into account. In the case of a solid boundary at $z = 0$, the averaged x- and y-momentum equations should be solved to obtain the mean tangential velocity in the boundary layer and, by taking its limit as the boundary-layer coordinate $Z \to \infty$, the slip velocity that serves as boundary condition for the interior equation (4.7). Let us consider the x-momentum equation, which reads

$$\rho_0 \nabla \cdot (\overline{u_1 \boldsymbol{u}_1}) = -\partial_x \bar{p}_2 + \mu \partial_{zz}^2 \bar{u}^{\mathrm{E}} + O(\delta),$$

when only the dominant viscous term is retained. Now, the contribution to the left-hand side of this equation that is associated with the potential part of $\boldsymbol{u}_1$ is balanced by the pressure gradient up to $O(\delta^2)$ (as it is in the interior). Subtracting this part leads to

$$\nu \partial_{zz}^2 \bar{u}^{\mathrm{E}} = \nabla \cdot (\overline{u_1 \boldsymbol{u}_1}) - \nabla \cdot \left(\overline{\partial_x \phi_1 \nabla \phi_1}\right) + O(\delta). \tag{4.8}$$

The boundary condition for this equation is obtained by averaging the no-slip condition on the (possibly moving) boundary and is

$$\bar{u}^{\mathrm{L}}(x, y, 0) = \bar{u}^{\mathrm{E}}(x, y, 0) + \overline{\boldsymbol{\xi}_1 \cdot \nabla u_1}(x, y, 0) = 0. \tag{4.9}$$

It is therefore convenient to solve, rather than (4.8), the equivalent equation for the Lagrangian mean flow, namely

$$\nu \partial_{zz}^2 \bar{u}^{\mathrm{L}} = \nabla \cdot (\overline{u_1 \boldsymbol{u}_1}) - \nabla \cdot \left(\overline{\partial_x \phi_1 \nabla \phi_1}\right) + \nu \partial_{zz}^2 \left(\overline{\boldsymbol{\xi}_1 \cdot \nabla u_1}\right) + O(\delta). \tag{4.10}$$

This computation, taking advantage of the boundary-layer scaling (3.8), is carried out in Appendix A. The result is

$$\begin{aligned} \frac{\omega}{2} \bar{u}^{\mathrm{L}} &= \frac{1}{4} \left[3(1+\mathrm{i}) \hat{U} \frac{\mathrm{d}\hat{U}^*}{\mathrm{d}x} + (1+2\mathrm{i}) \hat{V} \frac{\mathrm{d}\hat{U}^*}{\mathrm{d}y} + (2+\mathrm{i}) U \frac{\mathrm{d}\hat{V}^*}{\mathrm{d}y} \right] \left(\mathrm{e}^{-2Z} - 1\right) \\ &+ \frac{\mathrm{i}}{2} \left[\left(3\partial_{xx}^2 \hat{\phi} + \partial_{yy}^2 \hat{\phi} - \partial_{zz}^2 \hat{\phi}\right) \hat{U}^* + 2\partial_{xy}^2 \hat{\phi}\, V^* \right] \left(\mathrm{e}^{-(1+\mathrm{i})Z} - 1\right) + \mathrm{c.c.}, \end{aligned} \tag{4.11}$$

where all the functions of z are evaluated at $z = 0$. Note that $\bar{u}^{\mathrm{L}}$ is $O(1)$ throughout the boundary layer, in contrast with $\bar{u}^{\mathrm{E}}$ and $\bar{u}^{\mathrm{S}}$ which have (cancelling) $O(\delta^{-1})$ contributions. Taking the limit $Z \to \infty$ in (4.11) gives the slip velocity for the interior solution,

$$\begin{aligned} \frac{\omega}{2}\bar{u}^{\mathrm{L}}_{\mathrm{slip}} &= -\frac{1}{4}\left[3(1+\mathrm{i})\hat{U}\frac{\mathrm{d}\hat{U}^*}{\mathrm{d}x} + (1+2\mathrm{i})\hat{V}\frac{\mathrm{d}\hat{U}^*}{\mathrm{d}y} + (2+\mathrm{i})U\frac{\mathrm{d}\hat{V}^*}{\mathrm{d}y}\right] \\ &- \frac{\mathrm{i}}{2}\left[\left(3\partial^2_{xx}\hat{\phi} + \partial^2_{yy}\hat{\phi} - \partial^2_{zz}\hat{\phi}\right)\hat{U}^* + 2\partial^2_{xy}\hat{\phi}V^*\right] + \text{c.c.}, \end{aligned} \tag{4.12}$$

The slip velocity in the y-direction $\bar{v}^{\mathrm{L}}_{\mathrm{slip}}$ is given by an analogous expression with (x, y) and (U, V) interchanged. The normal component of the Lagrangian-mean velocity vanishes to leading order in the boundary layer. Thus the boundary conditions for the interior flow on a boundary $z = 0$ reads

$$\bar{\boldsymbol{u}}^{\mathrm{L}} = (\bar{u}^{\mathrm{L}}_{\mathrm{slip}}, \bar{v}^{\mathrm{L}}_{\mathrm{slip}}, 0) \quad \text{at} \quad z = 0. \tag{4.13}$$

4.3 Complete solution

Let us summarise how the Eulerian and Lagrangian mean flows in LSAW devices can be computed. Once the wave potential $\hat{\phi}$ has been obtained, in general by solving for the coupled linear motion of the fluid and underlying solid, the Stokes drift away from the boundary layers can be directly evaluated from its definition (2.9). The Eulerian mean flow is computed by solving (4.4) and (4.7), with the boundary condition implied by (4.13) and similar on other boundaries. The Lagrangian mean flow is then computed as the sum of the Eulerian mean flow and Stokes drift.

It is convenient to decompose the Eulerian mean flow according to

$$\bar{\boldsymbol{u}}^{\mathrm{E}} = \bar{\boldsymbol{u}}^{\mathrm{E}}_{\mathrm{i}} + \bar{\boldsymbol{u}}^{\mathrm{E}}_{\mathrm{b}}. \tag{4.14}$$

Here $\bar{\boldsymbol{u}}^{\mathrm{E}}_{\mathrm{i}}$ is the interior-driven part, which satisfies (4.4) and (4.7) and no-slip boundary conditions, and $\bar{\boldsymbol{u}}^{\mathrm{E}}_{\mathrm{b}}$ is the boundary-driven part, which satisfies (4.4) and the homogeneous version of (4.7), namely

$$\nabla^2\nabla \times \bar{\boldsymbol{u}}^{\mathrm{E}}_{\mathrm{b}} = 0, \tag{4.15}$$

with boundary conditions of the form

$$\bar{\boldsymbol{u}}^{\mathrm{E}}_{\mathrm{b}} = (\bar{u}^{\mathrm{L}}_{\mathrm{slip}}, \bar{v}^{\mathrm{L}}_{\mathrm{slip}}, 0) - \bar{\boldsymbol{u}}^{\mathrm{S}} \quad \text{at} \quad z = 0 \tag{4.16}$$

so that (4.13) is satisfied. Note that $\bar{\boldsymbol{u}}^{\mathrm{E}}_{\mathrm{b}}$ is driven by a combination of boundary-layer and Stokes-drift effects, and that it is not necessarily tangential to the boundary.

We can use the results of the previous sections to estimate the order of magnitude of the various contribution to the Lagrangian mean flow. Taking $\alpha \sim \boldsymbol{u}_1/c \sim \rho_1/\rho_0$ and assuming that ν and ν' have the same order of magnitude (as in water for instance) gives the estimate

$$\bar{\boldsymbol{u}}^{\mathrm{S}} \sim c\alpha^2. \tag{4.17}$$

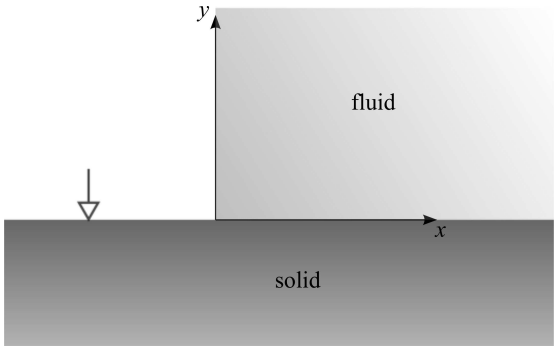

Figure 1: Configuration of the interacting fluid and solid considered in §§ 5–6. The surface acoustic waves in the solid are forced at the location indicated by the arrow.

for the Stokes drift (2.9). On the other hand, the interior-driven part of the Eulerian mean flow is estimated from (4.7) as

$$\bar{\boldsymbol{u}}_{\mathrm{i}}^{\mathrm{E}} \sim (\ell\kappa)^2 c\alpha^2. \tag{4.18}$$

Here ℓ is an 'outer scale', that is, the scale over which quadratic correlations such as $\overline{\rho_1 \boldsymbol{u}_1}$ vary; it is fixed by the size of the wave source or the smallest dimension of the fluid domain. Finally, it can be seen from (4.12) that the slip velocity is of the same order of magnitude as the Stokes drift, leading to the estimate

$$\bar{\boldsymbol{u}}_{i}^{\mathrm{E}} \sim c\alpha^2 \tag{4.19}$$

for the boundary-driven flow.

In practice, ℓ is determined by the size of the device, or by the size of the acoustic-wave source (e.g. the decay scale of LSAWs in LSAW-based devices), whichever is the smallest. If this is substantially larger than the wavelength of the acoustic waves, then the interior-driven Eulerian mean flow dominates the other contributions to the Lagrangian mean flow, and can be used as a proxy for the Lagrangian mean flow; if ℓ is just a few wavelengths, however, the interior-driven, boundary-driven and Stokes contributions should all be computed to estimate the Lagrangian mean flow accurately. Both situations are likely to arise in LSAW devices: in the experiments of Frommel et al. (2008*a*), for instance, ℓ is much larger than the wavelengths, while the channel device of Tan et al. (2009) is only a few wavelengths wide.

5 Fluid–solid coupling

We now examine the specifics of the generation of mean flows by LSAWs by considering the full coupling between the fluid and the underlying solid in a particular configuration. This configuration is motivated by the experimental work but taken as two-dimensional for simplicity: an isotropic linear elastic solid occupies the lower half plane $y < 0$, and a compressible fluid occupies the first quadrant $x > 0$, $y > 0$. Surface acoustic waves in the solid are generated at some $x \to -\infty$ and are scattered and refracted at the solid–fluid interface, leading to the

propagation of sound waves in the fluid which, in turn, generate a mean flow. See Figure 1 for a schematic.

5.1 Solid

The solid is modelled as an inviscid, isotropic, linear elastic solid. Although it is usual to write the governing equations for solids in terms of the displacement field, we use the velocity field instead so as to make a more complete parallel between the treatment of the fluid and solid. Decomposing the velocity field in the solid as

$$\boldsymbol{u}^{\mathrm{s}} = \nabla\phi^{\mathrm{s}} + \nabla^{\perp}\psi^{\mathrm{s}}, \tag{5.1}$$

where $\nabla^{\perp} = (-\partial_y, \partial_x)$, the potential and streamfunction satisfy the wave equations

$$\partial_{tt}^2\phi^{\mathrm{s}} = a^2\nabla^2\phi^{\mathrm{s}} \quad \text{and} \quad \partial_{tt}^2\psi^{\mathrm{s}} = b^2\nabla^2\psi^{\mathrm{s}}, \tag{5.2}$$

where a and b are the longitudinal and transverse wave speeds of the solid. These are given in terms of the Lamé parameters λ^{s} and μ^{s} and density ρ^{s} of the solid by

$$a = \sqrt{(\lambda^{\mathrm{s}} + 2\mu^{\mathrm{s}})/\rho^{\mathrm{s}}} \quad \text{and} \quad b = \sqrt{\mu^{\mathrm{s}}/\rho^{\mathrm{s}}}. \tag{5.3}$$

Here and in what follows, variables with the superscript s characterise the solid, while those with no superscripts continue to characterise the fluid.

We emphasise the difference between the spatial coordinates used to describe the motion in the fluid and in the solid: equations (2.1)–(2.2) for the fluid are written in Eulerian representation, with $\boldsymbol{x}$ representing fixed positions in space; in contrast, equations (5.2) are written in Lagrangian representation, with $\boldsymbol{x}$ labelling a particle by means of its position in the undeformed solid. The distinction is crucial when the boundary conditions matching the motion in the fluid to that in the solid are considered.

5.2 Boundary conditions

The wall bounding the liquid to the left is assumed rigid and fixed. Thus we impose the condition

$$\boldsymbol{u} = 0 \quad \text{for} \quad x = 0,\, y > 0 \tag{5.4}$$

on the fluid velocity. At the interface between the solid and air (treated as vacuum), the tangential and normal components of the stress tensor, which satisfy

$$\partial_t T^{\mathrm{s}} = \mu^{\mathrm{s}}\left(\partial_y u^{\mathrm{s}} + \partial_x v^{\mathrm{s}}\right) \quad \text{and} \quad \partial_t N^{\mathrm{s}} = \lambda^{\mathrm{s}}\left(\partial_x u^{\mathrm{s}} + \partial_y v^{\mathrm{s}}\right) + 2\mu^{\mathrm{s}}\partial_y v^{\mathrm{s}}, \tag{5.5}$$

vanish:

$$T^{\mathrm{s}} = N^{\mathrm{s}} = 0 \quad \text{for} \quad x > 0,\, y = 0. \tag{5.6}$$

To write down the boundary conditions at the fluid–solid interface, we use the fluid displacements $\boldsymbol{\xi}(\boldsymbol{x}, t)$ whose exact definition,

$$\partial_t\boldsymbol{\xi} + \boldsymbol{u}\cdot\nabla\boldsymbol{\xi} = \boldsymbol{u}, \tag{5.7}$$

Fluid (water)		
Density	ρ	10^3 kg m^{-3}
Sound speed	c	$1.5 \cdot 10^3$ m s^{-1}
Shear viscosity	μ	10^{-3} kg m^{-1} s^{-1}
Bulk viscosity	μ^{b}	$2.5 \cdot 10^{-3}$ kg m^{-1} s^{-1}
Solid		
Density	ρ^{s}	$4.65 \cdot 10^3$ kg m^{-3}
Longitudinal wave speed	a	$8 \cdot 10^3$ m s^{-1}
Transverse wave speed	b	$4.64 \cdot 10^3$ m s^{-1}
Forcing		
Angular frequency	ω	$9.425 \cdot 10^8$ s^{-1}

Table 1: Parameters used for the numerical application.

can be approximated by the linearisation $\partial_t \boldsymbol{\xi}_1 = \boldsymbol{u}_1$ already used in § 3. The continuity of the velocity field between fluid and solid is then written as

$$\boldsymbol{u}(\boldsymbol{x}', t) = \boldsymbol{u}^{\mathrm{s}}(\boldsymbol{x}, t) \quad \text{for} \quad x > 0,\, y = 0, \tag{5.8}$$

where $\boldsymbol{x}'$ is related to $\boldsymbol{x}$ according to

$$\boldsymbol{x}' = \boldsymbol{x} + \boldsymbol{\xi}(\boldsymbol{x}', t), \tag{5.9}$$

where $\boldsymbol{\xi}(\boldsymbol{x}', t)$ can be approximated by $\boldsymbol{\xi}_1(\boldsymbol{x}, t)$. Similarly, the continuity of the tangential and normal stresses read

$$T(\boldsymbol{x}', t) = T^{\mathrm{s}}(\boldsymbol{x}, t) \quad \text{and} \quad N(\boldsymbol{x}', t) = N^{\mathrm{s}}(\boldsymbol{x}, t) \quad \text{for} \quad x > 0,\, y = 0, \tag{5.10}$$

with T^{s} and N^{s} given in (5.5), and

$$T = \mu\,(\partial_y u + \partial_x v) \quad \text{and} \quad N = -p + (\mu + \mu')\partial_y v + (\mu' - \mu)\partial_x u. \tag{5.11}$$

As anticipated, the boundary-layer solution shows that (5.11) can be approximated as

$$T = O(\delta) \quad \text{and} \quad N = -p + O(\delta) \tag{5.12}$$

so that the fluid can be treated as inviscid in its interaction with the solid.

Note that expanding (5.8) in powers of α and averaging gives at $O(\alpha^2)$ the condition (4.9) of vanishing Lagrangian mean velocity at the boundary. There is obviously no mean velocity in the solid.

6 Results

We present results for the wave fields and mean flows obtained in the configuration sketched in Figure 1. The parameters have been chosen in rough agreement with those of the experiments

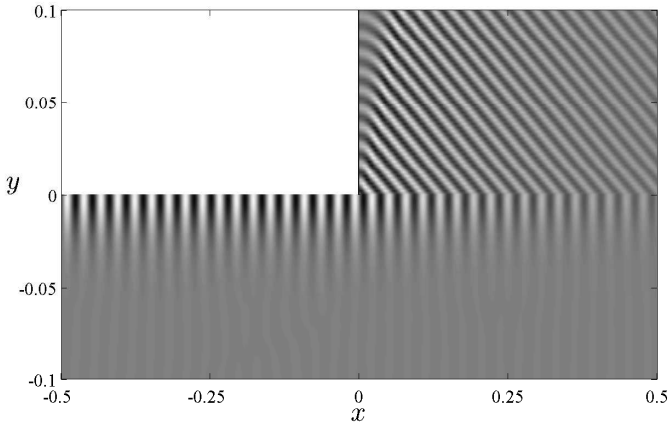

Figure 2: Wave field in the solid and fluid: the real part of the vertical velocity, $\mathrm{Re}\,\hat{v}$, is displayed in small domain around $(x, y) = (0, 0)$. Distances are in mm.

and numerical simulations of Frommel et al. (2008*b*) and Köster (2007); they are listed in Table 1. The liquid is water, at room temperature. The value used for its bulk viscosity differs from the value used in the references just mentioned and has been taken from recent experimental work by Dukhin & Goetz (2009).

Since the solid used in experiments is not isotropic, and thus characterised by more than two elastic moduli, we have chosen the value of the Lamé parameters to obtain a LSAW phase speed that is close to the observed speed. Specifically, we have taken $\lambda^{\mathrm{s}} = \mu^{\mathrm{s}} = 100$ N m^{-3} corresponding to the longitudinal and transverse wave speeds reported in Table 1. The dispersion relation of LSAWs can be written as

$$\left(2 - \frac{q^2}{b^2}\right)^2 - 4\sqrt{1 - \frac{q^2}{a^2}}\sqrt{1 - \frac{q^2}{b^2}} - \mathrm{i}\frac{\rho q^4}{\rho^{\mathrm{s}} b^4}\sqrt{\frac{1 - q^2/a^2}{q^2/c^2 - 1}} = 0, \tag{6.1}$$

where $q = \omega/k$ is the (complex) phase speed (e.g. Tew 1992, Craster 1996). For the parameters in Table 1 it has the solution $q = 4.27 - 5.4 \cdot 10^{-2}\,\mathrm{i}$, corresponding to a wavenumber

$$k_{\mathrm{LSAW}} = 2.2 \cdot 10^5 + 2.8 \cdot 10^3\,\mathrm{i\ m^{-1}} \tag{6.2}$$

and hence to LSAW wavelength and decay scale of about 29 μm and 720 μm, respectively. The speed of the LSAW is therefore

$$c_{\mathrm{LSAW}} = \omega/k = 4.3 \cdot 10^3\,\mathrm{m\ s^{-1}}. \tag{6.3}$$

6.1 Wave fields

To obtain the wave fields that result from the scattering of incident LSAWs, we solve the relevant coupled system of 3 coupled Helmholtz equations (2 in the solid, 1 in fluid) numerically. The simple geometry makes it possible to relate the velocities and stresses on the interface $y = 0$ to the potentials $\hat{\phi}(x, 0)$, $\hat{\phi}^{\mathrm{s}}(x, 0)$ and $\hat{\psi}^{\mathrm{s}}(x, 0)$ on this interface. These relationships involve

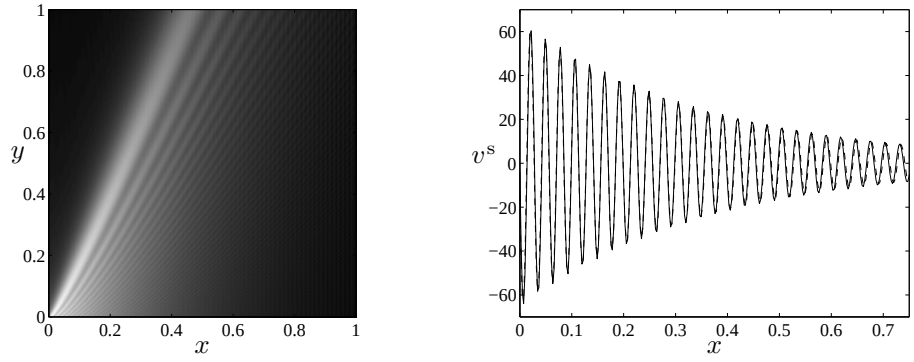

Figure 3: Wave amplitude in the fluid. Left: the potential $|\hat{\phi}|$ is shown for $(x, y) \in [0, 1] \times [0, 1]$ mm. Right: normal velocity of the interface (in mm s^{-1}) as a function of distance x (in mm); the numerical result (solid line) is compared with the form predicted for a pure LSAW (dashed line).

pseudodifferential operators that are best expressed using Fourier transforms in the x-direction. Using these, the problem can be reduced to one-dimensional pseudodifferential equations for $\hat{\phi}(x, 0)$, $\hat{\phi}^s(x, 0)$ and $\hat{\psi}^s(x, 0)$ which we solve using a pseudospectral discretisation (e.g. Trefethen 2000). Details about the numerical procedure are given in Appendix B.

We show in Figure 2 the wave field in both the solid and the fluid. The figure displays only a small portion of the computational domain: the full computational domain is 5 mm long in the x direction, with the forcing located around $x = -1.25$ mm (since we solve a one-dimensional problem, a grid in the y-direction is only needed for visualisation). The scattering appears relatively simple and dominated by the LSAWs, although other types of modes are no doubt excited (see Craster 1996, for an analogous problem). The exponential decay of the LSAWs as x increases from zero is clearly visible, but the viscous damping of the acoustic waves is not because the damping length is much larger than the domain plotted.

As discussed above, the solution satisfies the continuity of the normal velocity between the fluid and solid, but not the continuity of the tangential velocity. The thickness of the boundary layer that forms to ensure the continuity of the tangential velocity is computed form (3.5) and found to be $\delta = 46$ nm. With a wavenumber in the fluid given by $\kappa = \omega/c = 6.3 \cdot 10^5$ m^{-1}, the dimensionless parameter estimating both the validity of the boundary-layer approach and the importance of interior dissipation is $\delta\kappa = 3 \cdot 10^{-2}$. We emphasise that the use of the analytic form of the solution in the boundary layer avoids the need for the exceedingly high resolution that would be needed for a fully resolved numerical computation.

Figure 3 displays the amplitude $|\hat{\phi}|$ of the acoustic wave field in the fluid and provides a more detailed picture of the wave beam that is generated by the LSAW. The beam emanates from the corner $(x, y) = (0, 0)$, at an angle θ from the horizontal that can be computed from Snell's law $\cos\theta = c/c_{\mathrm{SAW}}$ as $\theta \approx 70°$. The figure shows a rather complicated interference pattern in the beam which results from the reflection on the rigid wall at $x = 0$.

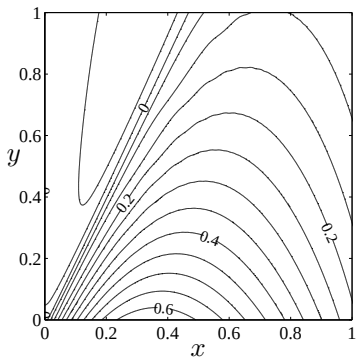

Figure 4: Streamfunction $\bar{\psi}^{\mathrm{S}}$ of the Stokes drift. Contour labels have units $10^{-3}\mathrm{mm}^2\,\mathrm{s}^{-1}$.

In spite of the scattering in the solid and of the reflection in the liquid, the form of the waves on the interface $y = 0$ is simple and well described by a pure LSAW. To illustrate this, we compare in Figure 3 the normal velocity $\mathrm{Re}\,\hat{v}(x,0) = \mathrm{Re}\,\hat{v}^{\mathrm{s}}(x,0)$ with that predicted for a LSAW with complex wavenumber (6.2). The amplitude and phase of the LSAW have been fitted to match the numerical result. The agreement is excellent. It should however be noted that details of the wave field on the interface, not necessarily distinguishable on the figure, encode the full solution in the fluid, including the interference pattern in Figure 3. Since the problem is linear, the amplitude of the interface displacements, of the order of 0.1 nm, is directly proportional to the strength of the forcing which we have chosen somewhat arbitrarily. We comment below on the magnitude of these displacement in connection with the amplitude of the mean flow generation.

6.2 Mean flows

We now consider the mean flows forced by the acoustic waves in the fluid. We start by the Stokes drift, which can be computed directly from the wave solution. Since the model is two-dimensional and the Stokes drift is approximately divergence-free (see (4.3)), it can be expressed in terms of a streamfunction $\bar{\psi}^{\mathrm{S}}$ according to

$$\bar{\boldsymbol{u}}^{\mathrm{S}} = \nabla^{\perp}\bar{\psi}^{\mathrm{S}} = (-\partial_y\bar{\psi}^{\mathrm{S}}, \bar{\partial}_x\bar{\psi}^{\mathrm{S}}). \tag{6.4}$$

Figure 4 shows this streamfunction and indicates that it corresponds to a jet aligned with the acoustic-wave beam. The maximum speed associated with the Stokes drift is found to be about $7\,\mu\mathrm{m\ s}^{-1}$. This is consistent with the scaling (4.17): with $\alpha = 4\cdot 10^{-5}$ (using a typical wave velocity of $50\,\mathrm{mm\ s}^{-1}$), this scaling gives typical Stokes velocities of the order of $2\,\mu\mathrm{m\ s}^{-1}$.

The Eulerian mean flow can also be written in terms of a streamfunction. The decomposition (4.14) into interior-driven and boundary-driven Eulerian mean flows reads

$$\bar{\psi}^{\mathrm{E}} = \bar{\psi}^{\mathrm{E}}_{\mathrm{i}} + \bar{\psi}^{\mathrm{E}}_{\mathrm{b}}. \tag{6.5}$$

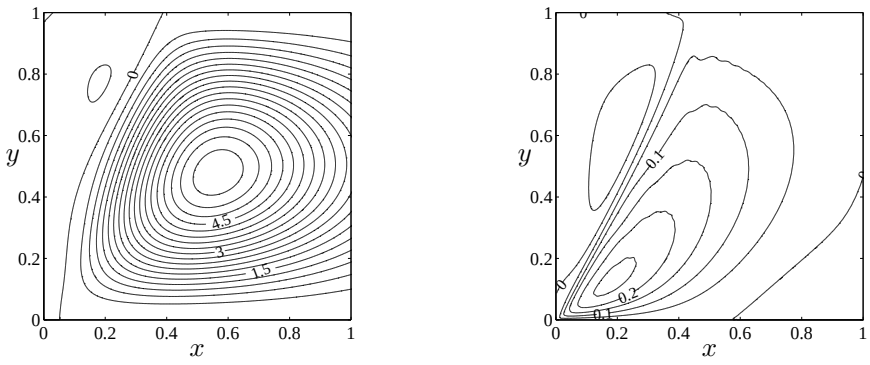

Figure 5: Left: streamfunction $\bar{\psi}_{\rm i}^{\rm E}$ of the interior-driven Eulerian mean flow. Contour labels have units mm^2 s^{-1}. Right: streamfunction $\bar{\psi}^{\rm L} + \bar{\psi}_{\rm b}^{\rm E}$ combining the Stokes drift and boundary-driven Eulerian mean flow. Contour labels have units 10^{-3}mm^2 s^{-1}.

The equations satisfied by $\bar{\psi}_{\rm i}^{\rm E}$ and $\bar{\psi}_{\rm b}^{\rm E}$ are obtained from (4.7) and (4.16) and given by

$$\nabla^4 \bar{\psi}_{\rm i}^{\rm E} = -\frac{\nu+\nu'}{\nu}\frac{\omega^2}{\rho_0 c^2}\nabla\times\overline{\rho_1 \boldsymbol{u}_1} \quad \text{with} \quad \bar{\psi}_{\rm i}^{\rm E} = \partial_n \bar{\psi}_{\rm i}^{\rm E} = 0 \quad \text{on the boundary,} \tag{6.6}$$

and

$$\nabla^4 \bar{\psi}_{\rm b}^{\rm E} = 0, \quad \text{with} \quad \bar{\psi}_{\rm b}^{\rm E} = -\bar{\psi}^{\rm S},\ \partial_n \bar{\psi}_{\rm i}^{\rm E} = -\partial_n \bar{\psi}^{\rm L} - \bar{u}_{\rm slip}^{\rm L} \quad \text{on the boundary.} \tag{6.7}$$

Here ∂_n denotes the derivative in the direction of the outward normal to the boundary, and $\bar{u}_{\rm slip}$ the slip velocity tangent to the boundary.

We have solved the two equations (6.6)–(6.7) using a finite-difference discretisation of the bi-Laplacian. The results depend strongly on the extent of the fluid domain in the y-direction. With the realistic values of the shear and bulk viscosities that we employ, the amplitude of the wave beam decreases over distances that are large compared to the typical size of experimental devices (the decay scale is estimated from (3.6) as $\gamma^{-1} \approx 2$ mm). As a result, treating the fluid domain as infinite in the y-direction would lead to an unrealistically strong Eulerian mean flow. We have therefore chosen to consider a bounded domain of size 1 mm in the y-direction. Since we use the wave field computed in a semi-infinite domain, we neglect the reflected beam that should appear on the upper boundary and whose amplitude is about 1/2 that of the main wave beam. The structure of the mean flow and its magnitude are not expected to be modified in an essential way by the reflected beam. In the x-direction, we continue to consider the domain as semi-infinite: the numerical computation requires to take a finite size, 2.5 mm for the reported here, but this has only little impact on the results.

Figure 5 shows the streamfunction $\bar{\psi}_{\rm i}^{\rm E}$ of the interior-driven Eulerian flow. The structure is similar to that observed in experiments and previous numerical models: a strong clockwise vortex is established to the right of the acoustic wave beam, with a much weaker counterclockwise circulation to the left. The qualitative features of this structure are relatively insensitive to the size of the domain, but the strength of the circulation is not. Here, the mean velocities obtained are of the order of 10 mm s^{-1}. These velocities are large compared to those reported in Köster

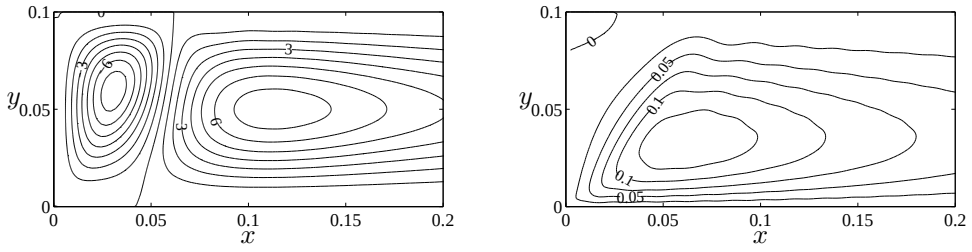

Figure 6: Left: streamfunction $\bar{\psi}_{\mathrm{i}}^{\mathrm{E}}$ of the interior-driven Eulerian mean flow in a domain with a boundary at $y = 0.1$ mm. Right: streamfunction $\bar{\psi}^{\mathrm{L}} + \bar{\psi}_{\mathrm{b}}^{\mathrm{E}}$ combining the Stokes drift and boundary-driven Eulerian mean flow. Contour labels have units $10^{-3}\,\mathrm{mm}^2\,\mathrm{s}^{-1}$.

(2007), even though the vertical displacement of the boundary that we have assumed is a factor 10 smaller than the displacements assumed in this paper for a similar set up. It is not clear what the reason for the differences may be, although it may be related to the lack of a treatment of the boundary layers in Köster (2007). We note that our numerical results are consistent with the scaling (4.18): using our earlier estimate $c\alpha \approx 2 \cdot 10^{-3}\,\mathrm{mm\ s}^{-1}$ and $\ell\kappa \sim 3 \cdot 10^2$ for $\ell = 1$ mm gives $\bar{\boldsymbol{u}}^{\mathrm{E}} \sim 20\,\mathrm{mm\,s}^{-1}$. Direct comparison with the velocities reported in experiments is difficult because the vertical displacements of the boundary are difficult to measure. It should also be borne in mind that lateral confinement, ignored in our two-dimensional set up, is also important for the amplitude of the mean velocity field, since it can reduce ℓ.

Since $\ell\kappa$ is large, the interior-driven mean flow dominates the Stokes drift and the boundary-driven flow. This is confirmed by the right panel of Figure 5 which shows the sum $\bar{\psi}^{\mathrm{L}} + \bar{\psi}_{\mathrm{b}}^{\mathrm{E}}$ of the two corresponding streamfunctions. By construction, this flow is tangential to the boundaries.[2] The largest velocities are reached near the boundary $y = 0$ and are of the order of $10\,\mu\mathrm{m\,s}^{-1}$, much smaller than the interior-driven velocities, as expected. The complete Lagrangian circulation is therefore very well approximated by the Eulerian circulation in Figure 5.

We emphasise that this is not a general feature of acoustic streaming in LSAW devices but one that depends on the geometry of the device: here, both the domain and the region of wave forcing provided by the LSAW are large compared to the acoustic wavelength, so that $\ell\kappa \gg 1$. If the domain is smaller, then the three contributions to Lagrangian mean flow can matter. We illustrate this by considering a domain of 0.1 mm in the y-direction instead of the 1 mm used so far. The size of the domain is now comparable to that used in the experiments of Tan et al. (2009). We continue to use the unbounded form of the acoustic waves in spite of the

[2] In principle, a two-dimensional boundary layer around the corner point $(x, y) = (0, 0)$ should be considered in order to obtain a Lagrangian velocity that is continuous along the boundary. This is not essential, however, since the full boundary-driven flow satisfies a Stokes equation whose solution is smooth in the interior even of the tangential velocity is discontinuous on the boundary.

strong reflections; the results should therefore be treated as illustrative rather than as proper predictions of the mean flows in the narrow domain. Figure 6 shows the streamfunctions $\bar{\psi}_{\mathrm{i}}^{\mathrm{E}}$ and $\bar{\psi}^{\mathrm{L}} + \bar{\psi}_{\mathrm{b}}^{\mathrm{E}}$. The interior-driven velocities reduced by a factor of the order of 10^3 compared to those in the larger domain, and although they still dominate the interior-driven contributions, it is only be a factor of 10 or so. As a result, the Lagrangian mean flow is not accurately approximated by the interior-drivem Eulerian flow only, in particular near the boundaries. This effect will be reinforced in domains that are smaller still, or that are confined in two or three directions.

7 Discussion

This paper is motivated by a series of recent experiments which have demonstrated the potential of streaming by leaky surface acoustic waves (LSAWs) to generate mixing flows in microfluidic devices (Moroney et al. 1991, Suri et al. 2002, Wixforth 2003, Guttenberg et al. 2004, Sritharan et al. 2006, Frommel et al. 2008*a*, Tan et al. 2009, Du et al. 2009, Yeo & Friend 2009). It discusses the computation of the Lagrangian mean flow, which controls the trajectories of fluid particles, for general wave-forcing protocols. The problem is formulated using the averaged vorticity equation, following Eckart (1948) and Westervelt (1953). This formulation extracts the balance between wave dissipation and mean-flow dissipation that is at the core of the streaming process by eliminating large, cancelling terms in the averaged momentum equation. Because of this, it appears preferable for numerical computations to the direct use of the momentum equation.

The formulation takes advantage of the weakness of the wave dissipation for realistic parameter values and employs a boundary-layer approach. In the interior of the fluid, the waves are irrotational and can be computed numerically by solving for a scalar potential. The waves have a significant vortical part only in thin boundary layers. Analytical expressions for the solution there are readily obtained in terms of the scalar potential, making it unnecessary to resolve the small-scale motion near the boundaries explicitly. The vortical part of the waves in the boundary layer contributes to the mean-flow generation in the form of an effective slip velocity that serves as boundary condition for the interior mean flow. We derive an expression for this slip velocity which takes into account the oscillatory motion of the boundary that forces the acoustic waves in the fluid.

The Lagrangian mean flow is the sum of the Stokes drift and of the Eulerian mean flow. The latter is naturally separated into two contributions: an interior-driven one, and a boundary-driven one which is associated with a combination of the slip velocity and Stokes drift at the boundary. We emphasise that the Stokes drift and boundary-driven Eulerian flows can be as large as the interior-driven Eulerian flow in LSAW devices if the size of the device is comparable to the acoustic wavelength.

Even when much smaller than the interior-driven flow, the boundary-driven flow can be important for a micromixer. As discussed by several authors, the no-slip boundary condition of viscous flows makes such flows inefficient mixers compared to slip flows (Lebedev & Turitsyn 2004, Salman & Haynes 2007, Gouillart et al. 2008). This is because the scalar to be mixed is

trapped near the boundary in a layer of thickness proportional to $\kappa^{1/4}$, where κ is the diffusivity of the scalar. However, flows driven by acoustic streaming can be expected to behave essentially as slip flows as far as mixing is concerned, because the boundary streaming results in a finite, viscosity-independent slip velocity immediately outside an exceedingly thin boundary layer. This is a potentially valuable property of LSAW mixers which deserves future investigation.

In this paper, we have followed most earlier work on streaming by LSAWs in treating the nonlinearity parameter α as small. However, in experiments such as those of Tan et al. (2009) and in our computations, mean velocities of the order of several millimetres per second are reached, corresponding to Reynolds numbers of order one. It would therefore be useful to assess the importance of the inertial terms on the mean flow. This is possible using an expansion based on a large Strouhal number $\omega\ell/\bar{u} \sim (\kappa\ell\alpha)^{-1}$ instead of small α. The developments in this case can be expected to be very similar to those presented in this paper, with the important difference that the inertial terms are retained in the mean-flow equations (e.g. Riley 2001). When inertial effects are important, the mean flows can become unstable and unsteady, leading to improved mixing performances.

Another possible extension of our results concerns streaming in very thin domains. This is motivated by experiments in which LSAWs generate mean flows in drops that are confined between two plates separated by a narrow gap (Guttenberg et al. 2004, Frommel et al. 2008*a*). The standard Hele–Shaw approximation (e.g. Batchelor 1967) can then be used to compute the interior-driven flow, but it would need to be extended to account for the non-uniform slip velocities that result from the boundary streaming on the plates.

Also of interest would be the development of a ray tracing approximation to the solution similar to that of Frommel et al. (2008*b*). The assumption of scale separation required for such an approach is valid in the bulk of the fluid, but special attention needs to be paid to possible diffraction effects as occur, in particular, at the corner $(x, y) = (0, 0)$ of our model. The ray-tracing approach should also take into account the all-important constraint of irrotationality of the acoustic waves in the fluid interior.

Finally, we note that the extreme thinness of the boundary layer (a few tens of nanometers) suggests that some non-negligible slip can occur at the fluid-solid interface. It would be interesting to analyse the possible consequences of such a slip by replacing the no-slip boundary condition used in this paper by a more sophisticated model such as the Navier boundary condition (e.g. Tabeling 2006).

Acknowledgements. JV acknowledges the support of a Leverhulme Research Fellowship and the hospitality of the Courant Institute where part of this research was carried out. He thanks J. Cosgrove for stimulating discussions.

A Mean flow in the boundary layers

In this Appendix, we solve the averaged momentum equation (4.10) in the boundary layer near $z = 0$. We start by writing (3.8) as

$$\boldsymbol{u}_1(z) = \boldsymbol{u}^{\phi}(z) + \boldsymbol{u}^{\psi}(Z),$$

where $\boldsymbol{u}^\phi = (u^\phi, v^\phi, w^\phi) = \nabla\phi_1$ is irrotational and $\boldsymbol{u}^\psi = (u^\psi, v^\psi, \delta w^\psi) = \delta\nabla\times\boldsymbol{\Psi}_1$ is divergence free, and where we have omitted the dependence on (x, y, t) for simplicity. The corresponding displacement fields are written as $\boldsymbol{\xi}^\phi = (\xi^\phi, \eta^\phi, \zeta^\phi)$ and $\boldsymbol{\xi}^\psi = (\xi^\psi, \eta^\psi, \delta\zeta^\psi)$. At this point, we treat all these fields as known exactly: it is only in the later stages of the derivation that their approximations up to $O(\delta)$ errors will be used. We will however use from the outset the approximations

$$\partial_{ZZ}^2 u^\psi = \frac{2}{\omega}\partial_t u^\psi + O(\delta^2) \quad \text{and} \quad \partial_{ZZ}^2 v^\psi = \frac{2}{\omega}\partial_t v^\psi + O(\delta^2), \tag{A.1}$$

which follow from (3.3), (3.5) and (3.9).

We now obtain the derivative $\partial_{zz}^2\left(\overline{\boldsymbol{\xi}_1\cdot\nabla u_1}\right)$ that appears on the right-hand side of (4.10). This contains three terms, computed as

$$\partial_{zz}^2\left(\overline{\xi_1\partial_x u_1}\right) = \delta^{-2}\left(\overline{-\frac{2}{\omega}u^\phi\partial_x u^\psi + \frac{2}{\omega}u^\psi\partial_x u^\phi + 2\partial_Z\xi^\psi\partial_{xZ}^2 u^\psi}\right) + O(\delta^{-1}), \tag{A.2}$$

$$\partial_{zz}^2\left(\overline{\eta_1\partial_y u_1}\right) = \delta^{-2}\left(\overline{-\frac{2}{\omega}v^\phi\partial_y u^\psi + \frac{2}{\omega}v^\psi\partial_y u^\phi + 2\partial_Z\eta^\psi\partial_{yZ}^2 u^\psi}\right) + O(\delta^{-1}), \tag{A.3}$$

and

$$\begin{aligned}\partial_{zz}^2\left(\overline{\zeta_1\partial_z u_1}\right) &= \delta^{-3}\left(\overline{-\frac{2}{\omega}w^\phi\partial_Z u^\psi}\right) \\ &+ \delta^{-2}\left(\overline{-\frac{4}{\omega}u^\psi\partial_z w^\phi - \frac{4}{\omega}u^\psi\partial_Z w^\psi - \frac{2}{\omega}w^\psi\partial_Z u^\psi + \partial_{ZZ}^2\zeta^\psi\partial_Z u^\psi}\right) + O(\delta^{-1}).\end{aligned} \tag{A.4}$$

The computation is straightforward, if tedious: it uses extensively integration by parts in time to eliminate the displacements in favour of the velocities, as well as (A.1) and its analogue for ξ^ψ and η^ψ to eliminate second derivatives in Z. Note that the $O(\delta^{-3})$ term in (A.4) implies that the leading-order approximations to w^ϕ and u^ϕ are insufficient to estimate (A.4) with the same $O(\delta^{-2})$ accuracy as (A.2)–(A.3). However, as shown below, this term is cancelled in the right-hand side of (4.10) by an equal and opposite contribution to $\nabla\cdot(\overline{u_1\boldsymbol{u}_1})$.

The other terms on the right-hand side of (4.10) are next obtained in the form

$$\begin{aligned}\nabla\cdot(\overline{u_1\boldsymbol{u}_1}) - \nabla\cdot\left(\overline{u^\phi\boldsymbol{u}^\phi}\right) &= \overline{2u^\psi\partial_x u^\phi + 2u^\phi\partial_x u^\psi + 2u^\psi\partial_x u^\psi} \\ &+\overline{v^\psi\partial_y u^\phi + u^\phi\partial_y v^\psi + v^\phi\partial_y u^\psi + u^\psi\partial_y v^\phi + v^\psi\partial_y u^\psi + u^\psi\partial_y v^\psi} \\ &+\delta^{-1}\overline{w^\phi\partial_Z u^\psi} + \overline{u^\psi\partial_z w^\phi + u^\phi\partial_Z w^\psi + w^\psi\partial_Z u^\psi + u^\psi\partial_Z w^\psi} + O(\delta)\end{aligned} \tag{A.5}$$

Rewriting (4.10) as

$$\frac{\omega}{2}\partial_{ZZ}^2\bar{u}^{\mathrm{L}} = \nabla\cdot(\overline{u_1\boldsymbol{u}_1}) - \nabla\cdot\left(\overline{u^\phi\boldsymbol{u}^\phi}\right) + \frac{\delta^2\omega}{2}\partial_{zz}^2\left(\overline{\boldsymbol{\xi}_1\cdot\nabla\boldsymbol{u}_1}\right) \tag{A.6}$$

using (3.5) and (3.9), and introducing the results (A.2)–(A.5) now leads to an explicit equation for the Lagrangian mean velocity $\bar{u}^{\mathrm{L}}$. Since this equation applies to the boundary layer, the z-dependent terms of (A.2)–(A.5) are evaluated at $z = 0$. After a number of simplifications, some involving the condition $\nabla\cdot\boldsymbol{u}^\psi = 0$, this equation can be written as

$$\begin{aligned}\frac{\omega}{2}\partial_{ZZ}^2\bar{u}^{\mathrm{L}} &= \overline{3u^\psi\partial_x u^\phi + 3u^\psi\partial_x u^\psi + u^\psi(\partial_y v^\phi + 2\partial_y v^\psi) + v^\psi(2\partial_y u^\phi + \partial_y u^\psi)} \\ &\overline{-u^\psi\partial_z w^\phi + \omega(\partial_Z\xi^\psi\partial_{xZ}^2 u^\psi + \partial_Z\eta^\psi\partial_{yZ}^2 u^\psi + \partial_{ZZ}^2\zeta^\psi\partial_Z u^\psi/2)} + O(\delta).\end{aligned} \tag{A.7}$$

As anticipated, the largest terms in (A.4) and (A.5) have cancelled out, and knowledge of the leading-order approximation to the wave fields is sufficient to obtain $\bar{u}^{\mathrm{L}}$ with negligible, $O(\delta)$ errors.

The right-hand side of (A.7) is made explicit by introducing the harmonic form of the wave solution. Specifically, we introduce $\boldsymbol{u}^{\phi} = \nabla\hat{\phi}_1 \mathrm{e}^{-\mathrm{i}\omega t} + \mathrm{c.c.}$, and

$$(u^{\psi}, v^{\psi}) = (-\partial_Z \hat{\Psi}^{(2)}, \partial_Z \hat{\Psi}^{(1)})\mathrm{e}^{-\mathrm{i}\omega t} + \mathrm{c.c.},$$

with the right-hand side given in (3.11), into (A.7). Only one term involves the vertical velocity w^{ψ} (or rather the vertical displacement ζ^{ψ}). This is expressed in terms of u^{ψ} and v^{ψ} using the incompressibility condition $\partial_Z w^{\psi} = -(\partial_x u^{\psi} + \partial_y v^{\psi})$. The result is

$$\begin{aligned} \frac{\omega}{2}\partial_{ZZ}^2 \bar{u}^{\mathrm{L}} &= \left[3(1+\mathrm{i})\hat{U}\frac{\mathrm{d}\hat{U}^*}{\mathrm{d}x} + (1+2\mathrm{i})\hat{V}\frac{\mathrm{d}\hat{U}^*}{\mathrm{d}y} + (2+\mathrm{i})U\frac{\mathrm{d}\hat{V}^*}{\mathrm{d}y}\right]\mathrm{e}^{-2Z} \\ &- \left[\left(3\partial_{xx}^2\hat{\phi} + \partial_{yy}^2\hat{\phi} - \partial_{zz}^2\hat{\phi}\right)\hat{U}^* + 2\partial_{xy}^2\hat{\phi}\,V^*\right]\mathrm{e}^{-(1+\mathrm{i})Z} + \mathrm{c.c.}. \end{aligned} \tag{A.8}$$

Integrating this equation twice with respect to Z, imposing $\bar{u}^{\mathrm{L}} = 0$ at $Z = 0$ and boundedness as $Z \to \infty$ finally leads to (4.11). We have verified (4.11) in the classical problems of a plane wave and a standing wave above a flat wall (e.g. Lighthill 1978*a*).

B Numerical method

To find the flow in the fluid interior, we need to solve (3.7) for the potential, together with the time-harmonic version of (5.2), namely

$$\nabla^2\hat{\phi}^{\mathrm{s}} = -\frac{\omega^2}{a^2}\hat{\phi}^{\mathrm{s}} \quad \text{and} \quad \nabla^2\hat{\psi}^{\mathrm{s}} = -\frac{\omega^2}{b^2}\hat{\psi}^{\mathrm{s}} \quad \text{for} \quad y < 0. \tag{B.1}$$

The boundary conditions obtained from those in § 5.2 are

$$\hat{T}^{\mathrm{s}} = 0 \quad \text{for} \quad y = 0, \tag{B.2}$$

$$\hat{N}^{\mathrm{s}} = 0 \quad \text{for} \quad y = 0, \quad x < 0, \tag{B.3}$$

$$\hat{N}^{\mathrm{s}} = -\hat{p} \quad \text{for} \quad y = 0,\ x > 0, \tag{B.4}$$

$$\hat{v}^{\mathrm{s}} = \hat{v} \quad \text{for} \quad y = 0,\ x > 0, \tag{B.5}$$

$$\hat{u} = 0 \quad \text{for} \quad x = 0,\ y > 0, \tag{B.6}$$

with the components of the stress tensor given by

$$\hat{T}^{\mathrm{s}} = \frac{\mathrm{i}\mu^{\mathrm{s}}}{\omega}(2\partial_{xy}^2\hat{\phi}^{\mathrm{s}} + \partial_{xx}^2\hat{\psi}^{\mathrm{s}} - \partial_{yy}^2\hat{\psi}^{\mathrm{s}}), \quad \hat{N}^{\mathrm{s}} = -\frac{\mathrm{i}\lambda^{\mathrm{s}}\omega}{a^2}\hat{\phi}^{\mathrm{s}} + \frac{2\mathrm{i}\mu^{\mathrm{s}}}{\omega}(\partial_{yy}^2\hat{\phi}^{\mathrm{s}} + \partial_{xy}^2\hat{\psi}^{\mathrm{s}})$$

and

$$-\hat{p} = -\mathrm{i}\omega\rho_0\hat{\phi}.$$

In numerical computations, we generate incident waves by imposing a non-zero $\hat{T}^{\mathrm{s}}$ on the boundary of the solid in a small interval around some for $x \ll -1$. We also handle the boundary

condition (B.6) by solving for the fluid in the whole upper half plane $y > 0$ and imposing the symmetry

$$\hat{\phi}(-x, y) = \hat{\phi}(x, y)$$

which implies that $\hat{u}(0, y) = \partial_x \hat{\phi}(0, y) = 0$.

The boundary-value problem (3.7), (B.1)–(B.6) determining the wave fields can be reduced to a one-dimensional problem using Fourier transforms to solve the interior equations (3.7) and (B.1) explicitly. Thus we write

$$\hat{\phi}^{\mathrm{s}}(x, y) = \int \check{\phi}^{\mathrm{s}}(k) \mathrm{e}^{\mathrm{i}kx + m_a y} \, \mathrm{d}k \quad \text{with} \quad \check{\phi}^{\mathrm{s}}(k) = \frac{1}{2\pi} \int \hat{\phi}^{\mathrm{s}}(x, 0) \mathrm{e}^{-\mathrm{i}kx} \, \mathrm{d}x, \tag{B.7}$$

$$\hat{\psi}^{\mathrm{s}}(x, y) = \int \check{\psi}^{\mathrm{s}}(k) \mathrm{e}^{\mathrm{i}kx + m_b y} \, \mathrm{d}k \quad \text{with} \quad \check{\psi}^{\mathrm{s}}(k) = \frac{1}{2\pi} \int \hat{\psi}^{\mathrm{s}}(x, 0) \mathrm{e}^{-\mathrm{i}kx} \, \mathrm{d}x, \tag{B.8}$$

$$\hat{\phi}(x, y) = \int \check{\phi}(k) \mathrm{e}^{\mathrm{i}(kx + my)} \, \mathrm{d}k \quad \text{with} \quad \check{\phi}(k) = \frac{1}{2\pi} \int \hat{\phi}(x, 0) \mathrm{e}^{-\mathrm{i}kx} \, \mathrm{d}x, \tag{B.9}$$

where

$$m_a = \sqrt{k^2 - \omega^2/a^2}, \quad m_b = \sqrt{k^2 - \omega^2/b^2}, \tag{B.10}$$

and

$$m = \sqrt{\frac{\omega^2}{c^2 - \mathrm{i}\omega(\nu + \nu')} - k^2}, \tag{B.11}$$

with a choice of branches such that $\operatorname{Re} m_a \geq 0$, $\operatorname{Re} m_b \geq 0$, $\operatorname{Im} m_a \leq 0$, $\operatorname{Im} m_b \leq 0$, $\operatorname{Re} m \geq 0$ and $\operatorname{Im} m \geq 0$ which ensures that, for $k \in \mathbb{R}$, decay or radiation boundary conditions are satisfied in the solid as $y \to -\infty$ and in the fluid as $y \to \infty$. (The branch choice is consistent with the causal limit $\omega \mapsto \omega + \mathrm{i}0^+$ with cuts avoiding the real k-axis.) Here, we have defined m_a and m_b differently from m: this is because our main interest is for LSAWs which are evanescent in the solid and propagating in the liquid and thus, with our definitions, are characterised by m_a, m_b and m with much larger real parts than imaginary parts for the scales k that are primarily excited.

With the definitions (B.7)–(B.9) it is straightforward to write down all fields in terms of $\check{\phi}^{\mathrm{s}}$, $\check{\psi}^{\mathrm{s}}$ and $\check{\phi}$, and hence in terms of (pseudodifferential transforms of) $\hat{\phi}^{\mathrm{s}}(x, 0)$, $\hat{\psi}^{\mathrm{s}}(x, 0)$ and $\hat{\phi}(x, 0)$. For instance,

$$\hat{v}(x, 0) = \partial_y \hat{\phi}(x, 0) = \mathrm{i} \int m \check{\phi}(k) \mathrm{e}^{\mathrm{i}kx} \, \mathrm{d}k = \frac{\mathrm{i}}{2\pi} \iint m \hat{\phi}(x, 0) \mathrm{e}^{\mathrm{i}k(x - x')} \, \mathrm{d}k \mathrm{d}x'.$$

Expressing the boundary conditions (B.2)–(B.5) in this manner reduces the boundary-value problem to a set of one-dimensional pseudo-differential equations for $\hat{\phi}^{\mathrm{s}}(x, 0)$, $\hat{\psi}^{\mathrm{s}}(x, 0)$ and $\hat{\phi}(x, 0)$. Solving these equations provides the velocity field in the solid and the potential part of the velocity field in the fluid up to $O(\delta)$ errors.

In principle, the equations could be solved analytically, using the Wiener–Hopf technique (Craster 1996). Here we solve it numerically, using a straightforward pseudospectral collocation method (Trefethen 2000). The infinite domain in x is replaced by a large periodic domain, and the three unknown fields $\hat{\phi}^{\mathrm{s}}(x, 0)$, $\hat{\psi}^{\mathrm{s}}(x, 0)$ and $\hat{\phi}(x, 0)$ are discretised on a regular grid. The pseudodifferential operators are then approximated by matrices which are computed using FFTs.

C McIntyre flow

In the absence of dissipation, the averaged Reynolds stresses associated with the acoustic waves are exactly balanced by a pressure gradient. As a result, a non-acceleration theorem holds and there is no interior forcing of the Eulerian mean flow $\bar{\boldsymbol{u}}^{\mathrm{E}}$. This flow does not vanish, however: because the no-normal-flow boundary condition to be satisfied applies to the Lagrangian mean flow, a non-zero $\bar{\boldsymbol{u}}^{\mathrm{E}}$ appears, driven by the boundary condition

$$\boldsymbol{n} \cdot \bar{\boldsymbol{u}}^{\mathrm{E}} = -\boldsymbol{n} \cdot \bar{\boldsymbol{u}}^{\mathrm{S}} \tag{C.1}$$

This flow, termed McIntyre flow by Lighthill (1978*b*) satisfies the two interior equations

$$\nabla \cdot \bar{\boldsymbol{u}}^{\mathrm{E}} = 0 \quad \text{and} \quad \nabla \times \bar{\boldsymbol{u}}^{\mathrm{E}} = 0 \tag{C.2}$$

obtained from (4.4) and (4.5). It is readily computed once the wave fields have been obtained and scales in the same way as the Stokes drift, i.e. $\bar{\boldsymbol{u}}^{\mathrm{E}} \sim c\alpha^2$.

The McIntyre flow can be thought of as resulting from the transient evolution which led to the steady wave patttern. It is established quickly, over a time scale of the order of the propagation of the acoustic waves across the fluid domain. In contrast, the dissipation-induced mean flow discsussed in this paper is established over the diffusive time scale ℓ^2/κ which is of the order of 1 second in a domain of 1 mm.

References

Antil, H., Glowinski, R., Hoppe, R. H. W., Linsenmann, C., Pan, T. & Wixforth, A. (2010), 'Modeling, simulation, and optimization of surface acoustic wave driven microfluidic biochips', *J. Comput. Math.* **28**, 149–169.

Batchelor, G. K. (1967), *An introduction to fluid dynamics*, Cambridge University Press.

Bradley, C. E. (1996), 'Acoustic streaming field structure: the influence of the radiator', *J. Acoust. Soc. Am.* **100**, 1399–1408.

Bühler, O. (2009), *Waves and mean flows*, Cambridge University Press.

Craster, R. V. (1996), 'A canonical problem for fluid–solid interfacial wave coupling', *Proc. R. Soc. Lond. A* **452**, 1695–1711.

Du, X. Y., Swanwick, M. E., Fu, Y. Q., Luo, J. K., Flewitt, A. J., Lee, D. S., Maeng, S. & Milne, W. I. (2009), 'Surface acoustic wave induced streaming and pumping in 128° Y-cut $LiNbO_3$ for microfluidic applications', *J. Micromech. Microeng.* **19**, 035016.

Dukhin, A. S. & Goetz, P. J. (2009), 'Bulk viscosity and compressibility measurement using acoustic spectroscopy', *J. Chem. Phys.* **130**, 1245219.

Eckart, C. (1948), 'Vortices and stream caused by sound waves', *Phys. Rev.* **73**, 68–76.

Frommel, T., Gogel, D., Kostur, M., Takner, P., Hänggi, P. & Wixforth, A. (2008*b*), 'Flow patterns and transport in Rayleigh surface acoustic wave streaming: combined finite element method and raytracing: numerics versus experiments', *IEEE Trans. Ultra. Ferr. and Freq. Cont.* **55**, 2299–2305.

Frommel, T., Kostur, M., Wenzel-Schäfer, M., Talkner, P., Hänggi, P. & Wixforth, A. (2008*a*), 'Microfluidic mixing via acoustically driven chaotic advection', *Phys. Rev. Lett.* **100**, 034502.

Gouillart, E., Dauchot, O., Dubrulle, B., Roux, S. & Thiffeault, J. (2008), 'Slow decay of concentration variance due to no-slip walls in chaotic mixing', *Phys. Rev. E* **78**, 026211.

Guttenberg, Z., Rathgeber, A., Rädler, J. O., Wixforth, A., Kostur, M., Schindler, M. & Talkner, P. (2004), 'Flow profiling of a surface acoustic pump', *Phys. Rev. E* **70**, 056311.

Köster, D. (2007), 'Numerical simulations of acoustic streaming on surface acoustic wave-driven biochips', *SIAM J. Sci. Comput.* **29**, 2352–2380.

Landau, L. D. & Lifschitz, E. M. (1987), *Fluid Mechanics*, 2nd edn, Pergamon.

Lebedev, V. V. & Turitsyn, K. S. (2004), 'Passive scalar evolution in peripheral regions', *Phys. Rev. E* **69**, 036301.

Lighthill, M. J. (1978*a*), 'Acoustic streaming', *J. Sound Vibr.* **61**, 391–418.

Lighthill, M. J. (1978*b*), *Waves in fluids*, Cambridge University Press.

Longuet-Higgins, M. S. (1953), 'Mass transport in water waves', *Phil. Trans. R. Soc. Lond. A* **245**, 535–581.

Moroney, R. M., White, R. M. & Howe, R. T. (1991), 'Microtransport induced by ultrasonic Lamb waves', *Appl. Phys. Lett.* **59**, 774–776.

Nguyen, N. & Wereley, S. (2002), *Fundamentals and applications of microfluidics*, Artech House.

Nyborg, W. L. (1953), 'Acoustic streaming due to plane attenuated waves', *J. Acoust. Soc. Am.* **25**, 68–75.

Nyborg, W. L. M. (1965), Acoustic streaming, *in* W. P. Mason, ed., 'Physical Acoustics', Vol. 2B, Academic Press, pp. 265–331.

Rayleigh, L. (1896), *Theory of Sound*, Vol. II, 2nd edn, Dover.

Riley, N. (2001), 'Steady streaming', *Ann. Rev. Fluid Mech.* **33**, 243–65.

Salman, H. & Haynes, P. H. (2007), 'A numerical study of passive scalar evolution in peripheral regions', *Phys. Fluids* **19**, 067101.

Squires, T. M. & Quake, S. R. (2005), 'Microfluidics: fluid physics at the nanoliter scale', *Rev. Mod. Phys.* **77**, 977–1026.

Sritharan, K., Strobel, C. J., Schneider, F., Wixforth, A. & Guttenberg, Z. (2006), 'Acoustic mixing at low Reynolds number', *Appl. Phys. Lett.* **88**, 054102.

Suri, C., Takenaka, K., Yanagida, H., Kojima, Y. & Koyama, K. (2002), 'Chaotic mixing generated by acoustic streaming', *Ultrasonics* **40**, 393–396.

Tabeling, P. (2006), *Introduction to microfluidics*, Oxford University Press.

Tan, M. K., Yeo, L. Y. & Friend, J. R. (2009), 'Rapid fluid flow and mixing induced in microchannels using surface acoustic waves', *Europhys. Lett.* **87**, 47003.

Tew, R. H. (1992), 'Non-specular phenomena at a fluid–solid boundary', *Proc. R. Soc. Lond. A* **437**, 433–449.

Trefethen, L. N. (2000), *Spectral methods in Matlab*, SIAM.

Westervelt, P. J. (1953), 'The theory of steady rotational flow generated by a sound field', *J. Acoust. Soc. Am.* **25**, 60–67.

Wiggins, S. & Ottino, J. M. (2004), 'Introduction: mixing in microfluidics', *Phil. Trans. R. Soc. London A* **362**, 923–935.

Wixforth, A. (2003), 'Acoustically driven planar microfluidics', *Superlattices and Microstructures* **33**, 389–389.

Yeo, L. Y. & Friend, J. R. (2009), 'Ultrafast microfluidics using surface acoustic waves', *Biomicrofluidics* **3**, 012002.